

The Higgs boson decay $h \rightarrow bs$ in the $U(1)_X$ SSM

Song Gao^{1,2,3}, Shu-Min Zhao^{1,2,3*}, Ming-Yue Liu^{1,2,3},

Xing-Yu Han^{1,2,3}, Xi Wang^{1,2,3}, Tai-Fu Feng^{1,2,3,4}

¹ *Department of Physics, Hebei University, Baoding 071002, China*

² *Hebei Key Laboratory of High-precision Computation and Application of Quantum Field Theory, Baoding, 071002, China*

³ *Hebei Research Center of the Basic Discipline for Computational Physics, Baoding, 071002, China and*

⁴ *Department of Physics, Chongqing University, Chongqing 401331, China*

(Dated: July 16, 2024)

Abstract

In the $U(1)_X$ SSM, we delve into the quark flavor violation of $h \rightarrow bs$, where h is identified as the SM-like Higgs boson discovered at the LHC. As the $U(1)$ extension of the minimal supersymmetric standard model (MSSM), the $U(1)_X$ SSM has new super fields such as right-handed neutrinos and three Higgs singlets. We conduct a thorough analysis of the underlying mechanisms and parameter dependencies of $h \rightarrow bs$ in the $U(1)_X$ SSM. In the $U(1)_X$ SSM, we discover that the $\text{Br}(h \rightarrow bs)$ for the Higgs decay to bs could significantly differ from the expectation in the standard model (SM), depending on the values of the new parameters introduced in the model. Our research not only contributes to a deeper understanding of Higgs physics within the $U(1)_X$ SSM, but also provides valuable guidance for new physics (NP).

PACS numbers:

Keywords: $U(1)_X$ SSM, Higgs boson, new physics

* zhaosm@hbu.edu.cn; 17713155332@163.com

I. INTRODUCTION

After the discovery of the Higgs boson[1–7], one of the main goals has been to measure its properties with the highest possible precision. Current measurements, within experimental and theoretical uncertainties, are consistent with the predictions of the SM for the Higgs boson. Flavor-changing Higgs interactions provide an intriguing scenario for searching for new physics. In the SM, flavor-changing neutral currents (FCNC) occur only at the loop level and are thus highly suppressed[8]. Therefore, physics beyond the SM may predict larger FCNC compared to the SM. The initial studies of the loop-induced hbs coupling originated in the 1980s[9], while more recent work based on current data reports that the predicted $\text{Br}(h \rightarrow bs)$ in the SM is approximately 10^{-7} [10–13].

Physicists have expanded the SM, resulting in a number of extended models, among which the Minimal Supersymmetric Standard Model (MSSM) has garnered significant attention. However, There are some problems with MSSM, including the μ -problem[14, 15] and the issue of massless neutrinos[16, 17]. To address these problems, we extend the MSSM by introducing the $U(1)_X$ gauge group, with the symmetry group being $SU(3)_C \times SU(2)_L \times U(1)_Y \times U(1)_X$ [18–21]. This extension adds three Higgs singlet superfields and right-handed neutrino superfields to the MSSM[22–24]. Consequently, there are five neutral CP-even Higgs component fields ($\hat{\eta}_1, \hat{\eta}_2, \hat{S}, H_u, H_d$) in the model, and mix together, forming a 5×5 mass-squared matrix. Consequently, the mass of the lightest CP-even Higgs particle can be improved at the tree level. In the $U(1)_X$ SSM, the small hierarchy problem in the MSSM is alleviated through the added right-handed neutrinos, sneutrinos, and extra Higgs singlets. The μ -problem existing in the MSSM is relieved after the spontaneous symmetry breaking of the S field in vacuum through $\lambda_H \hat{S} \hat{H}_u \hat{H}_d$. Through the term $Y_\nu \hat{\nu} \hat{H}_u$, the right-handed neutrinos and left-handed neutrinos mix together[25], which makes light neutrinos to obtain tiny masses through the seesaw mechanism.

Our work is to study quark flavor violating(QFV) decay. In Ref.[26], they study QFV interactions mediated by the Higgs boson h . Using an effective field theory approach, they systematically list all possible tree-level ultraviolet completions, which comprise models with vector-like quarks or extra scalars. Based on current limits from low-energy processes, such as meson mixing and $b \rightarrow s\gamma$, upper limits are provided for the allowed flavor-violating transitions. They find that flavor-violating transitions in scenarios with vector-like quarks are

always significantly suppressed[27, 28], while a general Two-Higgs-Doublet Model (2HDM) may have a considerable rate[29, 30]. They perform comprehensive numerical simulations, taking into account all relevant theoretical and phenomenological constraints. The results show that $\text{BR}(h \rightarrow bs)$ are still allowed at the subpercent (percent) level, which are being explored at the LHC. Meanwhile, the study of lepton flavor violation (LFV) is also crucial. In Refs.[31–33], they study Higgs-mediated flavor-changing neutral current interactions within the effective field theory approach, both with and without adopting the minimal flavor violation(MFV) hypothesis. These works have significantly contributed to our subsequent research on the $h \rightarrow bs$ decay in the $U(1)_X$ SSM work.

For flavor-changing couplings of $h \rightarrow bs$, bd , the LHC experiments have little direct sensitivity[34, 35]. The main decay channel of the Higgs is $h \rightarrow b\bar{b}$, which can mimic $h \rightarrow bs$ by mistagging one of the b-jets. Furthermore, it will not be possible to differentiate between jets from s and d quarks. Therefore, the Higgs decays to bs and bd are effectively indistinguishable. On the other hand, a huge QCD background causes trouble with processes involving bottom quarks. It makes the measurement of decays $h \rightarrow bj$, ($j = s, d$) very challenging at the LHC, even at HL-LHC.

To precisely measure the Higgs bosons' properties is one of the ILC's major physics goals. For the branching ratios of Higgs decays $h \rightarrow bs$, bd , the ILC could theoretically reach subpercent sensitivity[36]. Though these channels suffer from large QCD backgrounds and are hard or impossible to see at the LHC, they may be easily accessible in the ILC with clean collider environment.

The outline of this paper is as follows, in Sec.II, we will introduce the fundamental elements of the $U(1)_X$ SSM, including its superpotential, general soft-breaking terms. In Sec.III, we will provide analytical expressions for the branching ratio of the $h \rightarrow bs$ decay in the $U(1)_X$ SSM. In Sec.IV, we present the corresponding parameters and numerical analysis. In Sec.V, we offer a summary of this article. Some formulas are shown in the appendix.

II. THE RELEVANT CONTENT OF $U(1)_X$ SSM

The superpotential of $U(1)_X$ SSM is expressed as follows

$$W = l_W \hat{S} + \mu \hat{H}_u \hat{H}_d + M_S \hat{S} \hat{S} - Y_d \hat{d} \hat{q} \hat{H}_d - Y_e \hat{e} \hat{l} \hat{H}_d + \lambda_H \hat{S} \hat{H}_u \hat{H}_d$$

TABLE I: The superfields in $U(1)_X$ S SM

Superfields	\hat{q}_i	\hat{u}_i^c	\hat{d}_i^c	\hat{l}_i	\hat{e}_i^c	$\hat{\nu}_i$	\hat{H}_u	\hat{H}_d	$\hat{\eta}$	$\hat{\bar{\eta}}$	\hat{S}
$SU(3)_C$	3	$\bar{3}$	$\bar{3}$	1	1	1	1	1	1	1	1
$SU(2)_L$	2	1	1	2	1	1	2	2	1	1	1
$U(1)_Y$	1/6	-2/3	1/3	-1/2	1	0	1/2	-1/2	0	0	0
$U(1)_X$	0	-1/2	1/2	0	1/2	-1/2	1/2	-1/2	-1	1	0

$$+\lambda_C \hat{S} \hat{\eta} \hat{\bar{\eta}} + \frac{\kappa}{3} \hat{S} \hat{S} \hat{S} + Y_u \hat{u} \hat{q} \hat{H}_u + Y_X \hat{\nu} \hat{\eta} \hat{\nu} + Y_\nu \hat{\nu} \hat{l} \hat{H}_u. \quad (1)$$

We use the notations of v_u , v_d , v_η , $v_{\bar{\eta}}$ and v_S to signify the vacuum expectation values (VEVs) associated with the Higgs superfields H_u , H_d , v_η , $v_{\bar{\eta}}$, and S , respectively. Subsequently, we present the precise formulations of the two Higgs doublets and three Higgs singlets here

$$H_u = \begin{pmatrix} H_u^+ \\ \frac{1}{\sqrt{2}}(v_u + H_u^0 + iP_u^0) \end{pmatrix}, \quad H_d = \begin{pmatrix} \frac{1}{\sqrt{2}}(v_d + H_d^0 + iP_d^0) \\ H_d^- \end{pmatrix},$$

$$\eta = \frac{1}{\sqrt{2}}(v_\eta + \phi_\eta^0 + iP_\eta^0), \quad \bar{\eta} = \frac{1}{\sqrt{2}}(v_{\bar{\eta}} + \phi_{\bar{\eta}}^0 + iP_{\bar{\eta}}^0), \quad S = \frac{1}{\sqrt{2}}(v_S + \phi_S^0 + iP_S^0). \quad (2)$$

And two angles are defined as $\tan \beta = v_u/v_d$ and $\tan \beta_\eta = v_{\bar{\eta}}/v_\eta$.

The soft SUSY breaking terms of $U(1)_X$ S SM are as follows

$$\begin{aligned} \mathcal{L}_{soft} = & \mathcal{L}_{soft}^{MSSM} - B_S S^2 - L_S S - \frac{T_\kappa}{3} S^3 - T_{\lambda_C} S \eta \bar{\eta} + \epsilon_{ij} T_{\lambda_H} S H_d^i H_u^j \\ & - T_X^{IJ} \bar{\eta} \tilde{\nu}_R^I \tilde{\nu}_R^{*J} + \epsilon_{ij} T_\nu^{IJ} H_u^i \tilde{\nu}_R^{I*} \tilde{l}_j^J - m_\eta^2 |\eta|^2 - m_{\bar{\eta}}^2 |\bar{\eta}|^2 - m_S^2 S^2 \\ & - (m_{\tilde{\nu}_R}^2)^{IJ} \tilde{\nu}_R^{I*} \tilde{\nu}_R^J - \frac{1}{2} \left(M_S \lambda_X^2 + 2M_{BB'} \lambda_{\bar{B}} \lambda_X \right) + h.c. \end{aligned} \quad (3)$$

$\mathcal{L}_{soft}^{MSSM}$ represents the soft breaking terms of MSSM.

In the context of $U(1)_X$ S SM, the simultaneous existence of two Abelian groups, $U(1)_Y$ and $U(1)_X$, gives rise to a new effect that does not exist in MSSM: gauge kinetic mixing. This effect can also be induced through Renormalization Group Equations (RGEs), even if it is assumed as zero at M_{GUT} .

Y^Y denotes the $U(1)_Y$ charge, while Y^X represents the $U(1)_X$ charge. One can write the covariant derivatives of the $U(1)_X$ S SM in the following form[37–39]

$$D_\mu = \partial_\mu - i \begin{pmatrix} Y^Y, & Y^X \end{pmatrix} \begin{pmatrix} g_Y, & g'_{YX} \\ g'_{XY}, & g'_X \end{pmatrix} \begin{pmatrix} A'_\mu{}^Y \\ A'_\mu{}^X \end{pmatrix}, \quad (4)$$

where A_μ^Y and A_μ^X represent the gauge fields of $U(1)_Y$ and $U(1)_X$, respectively.

Under the condition that the two Abelian gauge groups remain unbroken, we employ the rotation matrix R to carry out a change of basis[39]

$$\begin{pmatrix} g_Y & g'_{YX} \\ g'_{XY} & g'_X \end{pmatrix} R^T = \begin{pmatrix} g_1 & g_{YX} \\ 0 & g_X \end{pmatrix}, \quad R \begin{pmatrix} A_\mu^Y \\ A_\mu^X \end{pmatrix} = \begin{pmatrix} A_\mu^Y \\ A_\mu^X \end{pmatrix}, \quad (5)$$

In the end, the covariant derivatives of the $U(1)_X$ SSM transform into

$$D_\mu = \partial_\mu - i \begin{pmatrix} Y^Y & Y^X \end{pmatrix} \begin{pmatrix} g_1 & g_{YX} \\ 0 & g_X \end{pmatrix} \begin{pmatrix} A_\mu^Y \\ A_\mu^X \end{pmatrix}. \quad (6)$$

At the tree level, three neutral gauge bosons A_μ^X , A_μ^Y , and V_μ^3 mix with each other, with their mass matrix represented in the basis of $(A_\mu^Y, V_\mu^3, A_\mu^X)$.

$$\begin{pmatrix} \frac{1}{8}g_1^2v^2 & -\frac{1}{8}g_1g_2v^2 & \frac{1}{8}g_1(g_{YX} + g_X)v^2 \\ -\frac{1}{8}g_1g_2v^2 & \frac{1}{8}g_1g_2v^2 & -\frac{1}{8}g_2(g_X + g_{YX})v^2 \\ (g_{YX} + g_X)v^2 & (g_{YX} + g_X)v^2 & \frac{1}{8}g_X^2\xi^2 \end{pmatrix}, \quad (7)$$

with $v^2 = v_u^2 + v_d^2$ and $\xi^2 = v_\eta^2 + v_{\bar{\eta}}^2$. Some mass matrices and coupling vertices are shown in Appendix A and Refs.[23, 25, 40].

III. PROCESS ANALYSIS

In this section, we investigate the amplitude and branching ratio of $h \rightarrow bs$. The corresponding Feynman diagrams are depicted in Fig.1. For example, we analyze one of the Feynman diagrams in Fig.1. The Feynman amplitude of Fig.1(a) is

$$\begin{aligned} \mathcal{M}_{(a)} = & \bar{U}_b(p) \int \frac{d^D k}{(2\pi)^D} \frac{1}{[(k+q)^2 - m_{\chi_k^0}^2][(p+q+k)^2 - m_{\tilde{d}_j}^2](k^2 - m_{\tilde{d}_i}^2)} \\ & \times \left((B_L P_L + B_R P_R)(\not{k} + \not{q} - m_{\chi^0})(A_L P_L + A_R P_R) \right) C_1 U_s(q). \end{aligned} \quad (8)$$

In this expression, p represents the momentum of the bottom quark (b), q corresponds to the momentum of the strange quark (s), and k is the loop momentum. The $m_{\tilde{d}_{i(j)}}$ term corresponds to the mass of the down-squark. $A_L, B_L, A_R,$ and B_R represent the coupling vertices mentioned in Section II. $\bar{U}_b(p)$ and $U_s(q)$ represent the wave functions of the bottom and strange quarks. C_1 is the coupling constant of $h\tilde{d}_i\tilde{d}_j$. The subscripts L and R represent

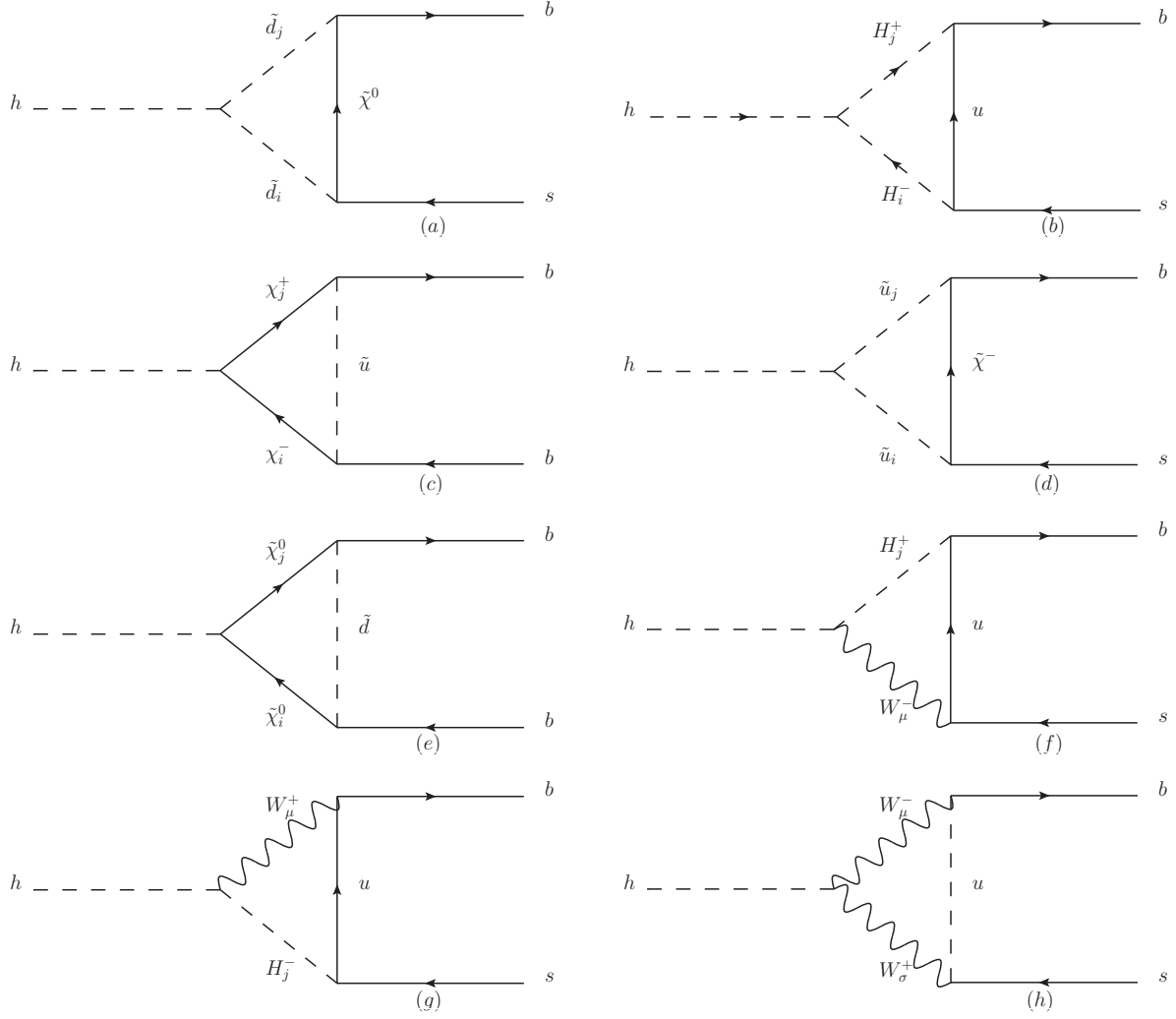


FIG. 1: Feynman diagrams for the $h \rightarrow bs$ process in the $U(1)_X$ SSM.

the left-handed and right-handed parts, respectively. In order to save space in the text, the detailed calculation process is shown in Appendix B.

The decay width Γ of $h \rightarrow bs$ is obtained by substituting $|\mathcal{M}|^2$ into the following formula[8]

$$\Gamma(h \rightarrow bs) = 2N_c \frac{\lambda^{\frac{1}{2}}(m_h^2, m_b^2, m_s^2)}{16\pi m_h^3} |\mathcal{M}|^2, \quad (9)$$

here, $N_c = 3$ is a color factor, $\lambda(x, y, z) = (x - y - z)^2 - 4y^2z^2$.

The branching ratio we obtained is

$$Br(h \rightarrow bs) = \frac{\Gamma(h \rightarrow bs)}{\Gamma(h)}. \quad (10)$$

Here, $\Gamma(h) = 4.1 \times 10^{-3} \text{GeV}$ [41].

IV. NUMERICAL ANALYSIS

In analyzing the numerical values, we consider the experimental constraints to study the flavor-changing neutral current process $h \rightarrow bs$, subject to the following restrictions.

1. The mass of the lightest CP-even Higgs, designated as m_h , approximately equals 125.25 GeV[42]. Our results of $\text{Br}(h \rightarrow bs)$ fall within the 3σ range of the Higgs boson mass. Currently, the mass of the Higgs boson, with 3σ level errors, is obtained

$$m_h = 125.25 \pm 0.51 \text{ GeV}. \quad (11)$$

2. The Higgs h decays($h \rightarrow \gamma + \gamma, Z + Z, W + W, b + \bar{b}, \tau + \bar{\tau}$)[29] should be satisfied.

3. Muon anomalous magnetic dipole moment is also taken into account[43, 44].

4. According to the latest LHC data[45–50], we take for the scalar lepton mass greater than 600 GeV, the chargino mass greater than 1000 GeV, and the masses of up-squarks and down-squarks greater than 1400 GeV.

In the calculations, we take the up quark mass $m_u = 0.0022$ GeV, the down quark mass $m_d = 0.0047$ GeV, the strange quark mass $m_s = 0.095$ GeV, the bottom quark mass $m_b = 4.18$ GeV, the charm quark mass $m_c = 1.275$ GeV, the top quark mass $m_t = 173.5$ GeV, the W boson mass $m_W = 80.385$ GeV, the Z boson mass $m_Z = 91.188$ GeV, the electron mass $m_e = 0.500$ MeV, the muon mass $m_\mu = 0.105$ GeV, $\alpha(m_Z) = 1/128$, $\alpha_s(m_Z) = 0.118$.

We use images to visualize the effects of variables on the results, where the quantitative parameters are set as follows

$$\begin{aligned} \mu &= 0.8 \text{ TeV}, \quad M_S = 3.6 \text{ TeV}, \quad v_S = 4.3 \text{ TeV}, \quad \kappa = 0.1, \quad \lambda_C = -0.08, \\ M_{\tilde{q}_{11}}^2 &= M_{\tilde{q}_{22}}^2 = 1.9^2 \text{ TeV}^2, \quad M_{\tilde{u}_{11}}^2 = M_{\tilde{u}_{22}}^2 = 1.9^2 \text{ TeV}^2, \quad M_{\tilde{q}_{33}}^2 = M_{\tilde{u}_{33}}^2 = 6 \text{ TeV}^2. \end{aligned} \quad (12)$$

To streamline the numerical investigation, we use the interdependency of the parameters, which undergo variations throughout the subsequent numerical analysis

$$\begin{aligned} g_X, \quad g_{YX}, \quad \tan\beta, \quad \lambda_H, \quad M_1, \quad M_2, \\ M_{BL}, \quad M_{BB'}, \quad M_{\tilde{d}_{ij}}^2 = M_{\tilde{d}_{ji}}^2, \quad (i, j = 1, 2, 3, i \neq j). \end{aligned} \quad (13)$$

Typically, the non-diagonal elements of the parameters are set to zero as a default, unless explicitly stated otherwise.

A. one-dimensional line graph

In this subsection, we conduct numerical calculations for $\text{Br}(h \rightarrow bs)$ and plot correlation graphs for various parameters to clearly illustrate the numerical results. We use the parameters as $\tan \beta = 13$, $M_1 = 0.7$ TeV, $M_2 = 1.2$ TeV, $(M_d)_{11}^2 = (M_d)_{22}^2 = (M_d)_{33}^2 = 2.70$ TeV², $M_{BL} = 0.7$ TeV, $M_{BB'} = 0.4$ TeV. These adopted parameter values are representative, and the obtained branching ratios of $h \rightarrow bs$ are at the order of 10^{-3} , which are the numerical results with a high probability. It may be easier to be measured at HL-LHC and future colliders.

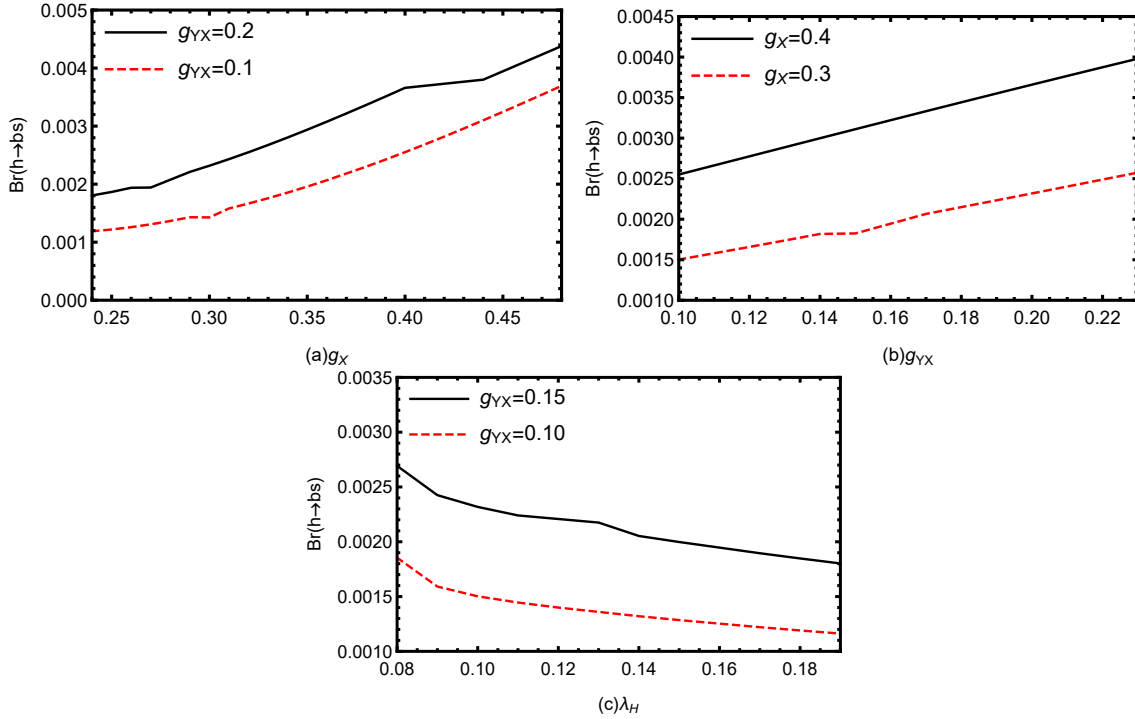


FIG. 2: The influence of various parameters on $\text{Br}(h \rightarrow bs)$: In (a) and (b), $\lambda_H = 0.1$, and in (c), $g_X = 0.3$.

g_X is the coupling constant of the new gauge $U(1)_X$. g_X appears in the particle mass matrixes and coupling vertexes, so it can improve the new physics effect. Obviously, g_X should be a sensitive parameter. In the Fig.2 (a), we plot $\text{Br}(h \rightarrow bs)$ versus g_X by the black-solid line($g_{YX} = 0.2$) and red-dashed line($g_{YX} = 0.1$) with $\lambda_H = 0.1$. We observe that, within the g_X range from 0.24 to 0.48, the corresponding values of the lines gradually increase with the increasing g_X . The obtained numerical results of $\text{Br}(h \rightarrow bs)$ are in the region (0.0015~0.006).

Through data analysing, we plot the relationship between g_{YX} and $\text{Br}(h \rightarrow bs)$ in Fig.2(b). In the context of $U(1)_X$ SSM, g_{YX} is the mixing gauge coupling constant beyond MSSM, which affects the strength of the coupling vertices. The study of g_{YX} is of interest. To investigate its impact on the $\text{Br}(h \rightarrow bs)$, we vary g_{YX} within the range of (0.1–0.24). and the values also increase when g_{YX} turns large. The characteristics of Fig.2(a) are similar as those of Fig.2(b). That is to say, g_X and g_{YX} have the similar effects to a certain extent.

λ_H comes from the term $\lambda_H S H_u H_d$ in the superpotential. The mass matrixes of several particles(chargino, neutralino, down-squark, up-squark, neutral Higgs, charged Higgs) all have the important parameter λ_H , which possibly produces complex effects on the numerical results. The contribution from each diagram in the Fig.1 is influenced by λ_H . Fig.2 (c) represents the relationship between λ_H and $\text{Br}(h \rightarrow bs)$. Within the λ_H range of 0.08 to 0.19, the corresponding values of the lines decrease as λ_H increases. This characteristic should be the result of competition of different contributions from the one-loop diagrams. In the whole, the value of $\text{Br}(h \rightarrow bs)$ falls within the range of $(1 \sim 6) \times 10^{-3}$ from the three diagrams in the Fig.2.

B. two-dimensional scatter plot

To better study the influence of parameters, we draw some multidimensional scatter plots based on χ^2 and select values that fall within 3σ range of χ^2 , ensuring a more significant correlation between the variables and $\text{Br}(h \rightarrow bs)$. We utilize the simplified expression of χ^2 as

$$\chi^2 = \sum_i \left(\frac{\mu_i^{th} - \mu_i^{exp}}{\delta_i} \right)^2. \quad (14)$$

In Eq.(14), μ_i^{th} signifies the theoretical value for the corresponding procedure derived within $U(1)_X$ SSM. The experimental data is denoted as μ_i^{exp} , while δ_i represents the error encompassing both statistical and systematic components.

The specific expression of χ^2 is presented as

$$\begin{aligned} \chi^2 = & \left(\frac{m_h^{th} - m_h^{exp}}{\delta_{m_h}} \right)^2 + \left(\frac{\mu_{\gamma\gamma}^{th} - \mu_{\gamma\gamma}^{exp}}{\delta_{\gamma\gamma}} \right)^2 + \left(\frac{\mu_{ZZ}^{th} - \mu_{ZZ}^{exp}}{\delta_{ZZ}} \right)^2 \\ & + \left(\frac{\mu_{WW}^{th} - \mu_{WW}^{exp}}{\delta_{WW}} \right)^2 + \left(\frac{\mu_{bb}^{th} - \mu_{bb}^{exp}}{\delta_{bb}} \right)^2 + \left(\frac{\mu_{\tau\bar{\tau}}^{th} - \mu_{\tau\bar{\tau}}^{exp}}{\delta_{\tau\bar{\tau}}} \right)^2 + \left(\frac{\Delta a_\mu^{th} - \Delta a_\mu}{\delta_{\Delta a_\mu}} \right)^2. \end{aligned} \quad (15)$$

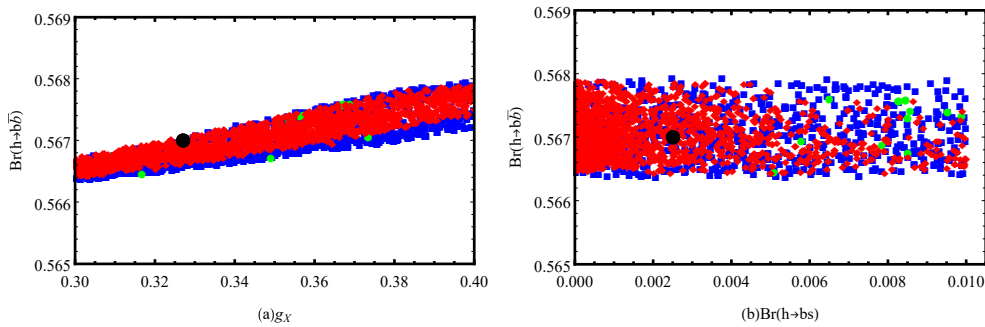
TABLE II: Scanning parameters for Fig.3, Fig.4, Fig.5 and Fig.6.

Parameters	g_X	g_{YX}	$\tan \beta$	M_1/ TeV	M_2/ TeV	M_{BL}/ TeV	$M_{BB'}/ \text{TeV}$	M_d^2/ TeV^2
Min	0.3	0.01	8	0.2	1	0.1	0.1	4
Max	0.4	0.3	35	1	2	1	1	16

The averaged values of the experimental data are derived from the updated PDG [20], $m_h^{exp} = 125.25 \pm 0.17 \text{ GeV}$, $\mu_{\gamma\gamma}^{exp} = 1.10 \pm 0.07$, $\mu_{ZZ}^{exp} = 1.01 \pm 0.07$, $\mu_{WW}^{exp} = 1.19 \pm 0.12$, $\mu_{bb}^{exp} = 0.98 \pm 0.12$, $\mu_{\tau\bar{\tau}}^{exp} = 1.15 \pm 0.15$. $\Delta a_\mu = (2.50 \pm 0.48) \times 10^{-9}$ is obtained from the latest work of muon g-2 [30-31].

We randomly scan eight parameters and present them in Table II. Fig.3, Fig.4, Fig.5 and Fig.6 are plotted using the parameters present in Table II. \blacklozenge is a value located within the 1σ range of χ^2 in the domain of $\chi^2 \leq 14.41$. \blacksquare is a value situated within the 2σ range of χ^2 , where $14.41 \leq \chi^2 \leq 20.89$. \bullet is a value situated within the 3σ range of χ^2 , where again $20.89 \leq \chi^2 \leq 28.65$. \bullet represents the value corresponding to the optimal point.

We chose two parameters to plot $\text{Br}(h \rightarrow b\bar{b})$, which are g_X and $\text{Br}(h \rightarrow bs)$. In Fig.3 (a), when g_X increases, $\text{Br}(h \rightarrow b\bar{b})$ has an upward trend, and remain in the 1σ range of SM prediction; In Fig.3 (b), most of the points are in the order of 10^{-3} of $\text{Br}(h \rightarrow bs)$, and the points of $\text{Br}(h \rightarrow b\bar{b})$ are in the range of $(0.565 - 0.568)$.


 FIG. 3: (a) $\text{Br}(h \rightarrow b\bar{b})$ versus g_X ; (b) $\text{Br}(h \rightarrow b\bar{b})$ versus $\text{Br}(h \rightarrow bs)$.

Subsequently, from eight parameters, we select two sensitive parameters g_{YX} and $\tan \beta$ to show the results, and plot the graphs respectively using g_{YX} and $\tan \beta$ as the horizontal axes and $\text{Br}(h \rightarrow bs)$ as the vertical axis in Fig.4. These two parameters exhibit significant influence on $\text{Br}(h \rightarrow bs)$. As seen in Fig.4(a), most of the points are distributed within the range of $0.05 \leq g_{YX} \leq 0.20$ and $10^{-4} \leq \text{Br}(h \rightarrow bs) \leq 10^{-2}$. When $g_{YX} \geq 0.2$ and

$\text{Br}(h \rightarrow bs) \leq 10^{-4}$, the density of points gradually decreases. In Fig.4(b), the majority of points are situated within the range of $11 \leq \tan \beta \leq 29$ and $5 \times 10^{-4} \leq \text{Br}(h \rightarrow bs) \leq 0.01$. When $15 \leq \tan \beta \leq 20$ and $\text{Br}(h \rightarrow bs) \leq 5 \times 10^{-4}$, the distribution of points becomes less dense. By combining the insights from Fig.4(a) and Fig.4(b), it is evident that when $g_{YX} \approx 0.20$ and $\tan \beta \approx 12$, χ^2 reaches its optimal value, resulting in $\text{Br}(h \rightarrow bs)$ of 2.5×10^{-3} .

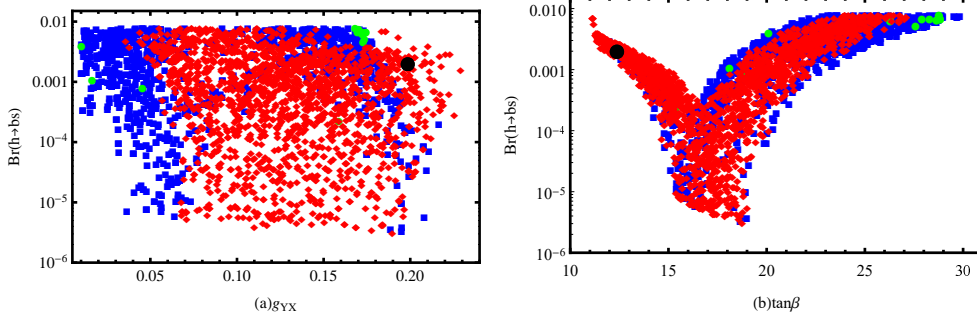


FIG. 4: (a) The χ^2 plot in the g_{YX} - $\text{Br}(h \rightarrow bs)$ plane; (b) The χ^2 plot in the $\tan \beta$ - $\text{Br}(h \rightarrow bs)$ plane.

Here, in Fig.5(a), we present a scatter plot of m_h with $\text{Br}(h \rightarrow bs)$. It can be observed that the optimal point of χ^2 is located near $m_h = 125.2$ GeV, which aligns well with the mass of the CP-even Higgs. As the mass of m_h increases or decreases from 125.2 GeV within the 3σ range, the density of points gradually enhances, and the points also cluster around the $\text{Br}(h \rightarrow bs)$ at the order of 10^{-3} . Fig.5(b) depicts a scatter plot of χ^2 with $\text{Br}(h \rightarrow bs)$, clearly illustrating the distribution of $\text{Br}(h \rightarrow bs)$ as χ^2 varies.

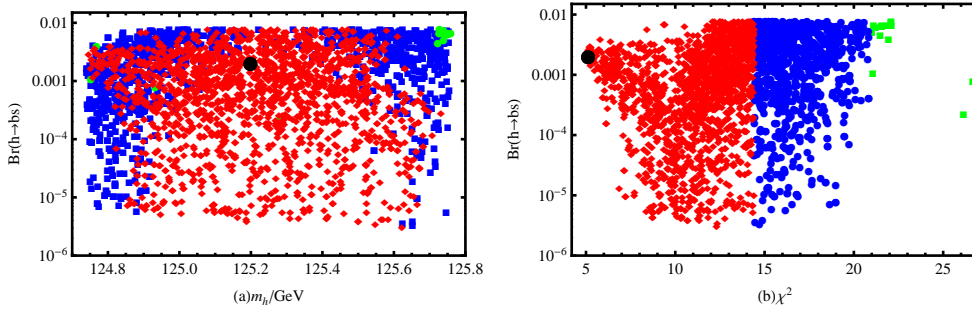


FIG. 5: (a) The χ^2 plot in the m_h - $\text{Br}(h \rightarrow bs)$ plane; (b) The χ^2 plot in the χ^2 - $\text{Br}(h \rightarrow bs)$ plane.

C. the Significant Impact of a_μ on Numerical Calculations

Next, we investigate the relation of muon magnetic dipole moment (MDM) with the flavor violation of $h \rightarrow bs$. The E989 collaboration at Fermilab [51] report the latest experimental data as $a_\mu^{FNAL} = 116592055(24) \times 10^{-11}$. The new averaged experiment value of muon MDM is $a_\mu^{exp} = 116592059(22) \times 10^{-11}$. Therefore, there is a deviation of 5.0σ between the experiment and SM expectation ($\Delta a_\mu = a_\mu^{exp} - a_\mu^{SM} = 249(48) \times 10^{-11}$)[52].

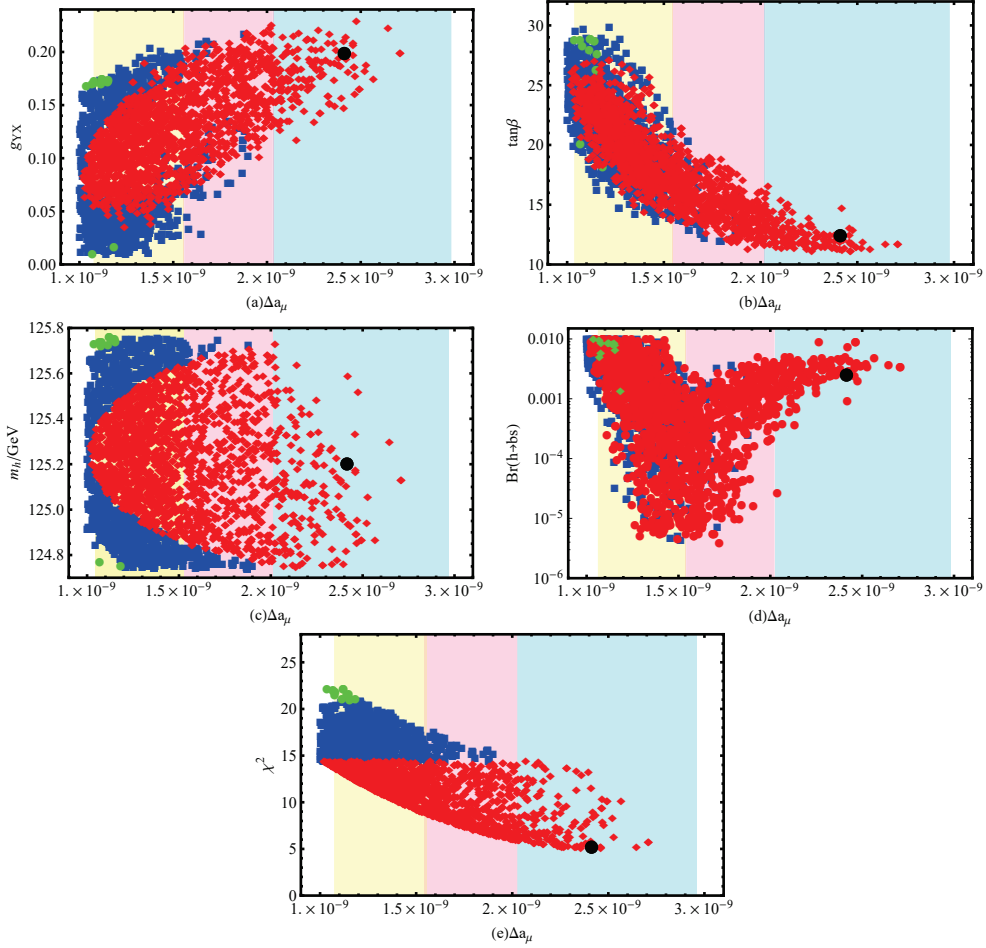


FIG. 6: The relation of Δa_μ with other parameters

In Fig.6, we present a series of scatter plots to illustrate the correlations between $\tan \beta$, m_h , g_{YX} , $\text{Br}(h \rightarrow bs)$, χ^2 , and Δa_μ . To clarify, the blue portion represents the 1σ ($2.02 \times 10^{-9} \leq \Delta a_\mu \leq 2.98 \times 10^{-9}$) range of Δa_μ , the pink portion represents the 2σ ($1.54 \times 10^{-9} \leq \Delta a_\mu \leq 2.02 \times 10^{-9}$) range, and the yellow portion represents the 3σ ($1.06 \times 10^{-9} \leq \Delta a_\mu \leq 1.54 \times 10^{-9}$) range. We can easily observe that the numerical results of χ^2 are all within the 3σ

experimental limit of Δa_μ , and the χ^2 optimal point is located at the $1\sigma(2.02 \times 10^{-9} \leq \Delta a_\mu \leq 2.50 \times 10^{-9})$ position of Δa_μ . In the area $\Delta a_\mu \in [(2.50 + 0.48), (2.50 + 1.44)] \times 10^{-9}$, there are no points in our used parameter space. So we do not show them. These diagrams indicate that when we take the optimal value of χ^2 , the numerical results of Δa_μ can effectively compensate for the deviation between the experimental data and the SM predictions.

The Fig.6(a) is plotted in the plane of Δa_μ versus g_{YX} . In the Fig.6(a), there are a lot more \blacklozenge and \blacksquare than \bullet , and their distribution is basically symmetrical. More points are located in the middle and left region. In the top right corner, there are \blacklozenge and \bullet . It implies that large g_{YX} leads to large Δa_μ . The Fig.6(b) shows the relation between Δa_μ and $\tan \beta$, where the outline of the points gradually decreases with enlarging Δa_μ . In our used parameter space, Δa_μ is the decreasing function of $\tan \beta$. The diagram of m_h versus Δa_μ is shown by the Fig.6(c). The image of the points is almost symmetrical with respect to the line $m_h = 125.25\text{GeV}$. The interior is \blacklozenge , and outwards are \blacksquare and \bullet in turn. The relationship between Δa_μ and $\text{Br}(h \rightarrow bs)$ is worth discussing, which is expressed by Fig.6(d). With the scanned parameters, when Δa_μ is larger than 1.5×10^{-9} , Δa_μ and $\text{Br}(h \rightarrow bs)$ present the relationship of the increasing function. With deep analysis, both Δa_μ and $\text{Br}(h \rightarrow bs)$ are increasing functions of g_{YX} as discussed in the front. On the other hand, they are both decreasing functions of $\tan \beta$. In the scanned parameter space, g_{YX} and $\tan \beta$ are sensitive parameters, which affect Δa_μ and $\text{Br}(h \rightarrow bs)$ obviously. In the whole, Δa_μ and $\text{Br}(h \rightarrow bs)$ show the same trend, when they vary with g_{YX} and $\tan \beta$. Therefore, as Δa_μ improves, the prediction for the $\text{Br}(h \rightarrow bs)$ increases. In the Fig.6(e), when Δa_μ turns large, χ^2 shrinks gradually.

The parameters $\tan \beta$, m_h , and g_{YX} are still significant factors that have a considerable impact on $\text{Br}(h \rightarrow bs)$. Compared to the previous section, after adding restrictions of Δa_μ , we obtain more precise parameter spaces.

V. CONCLUSION

In the $U(1)_X\text{SSM}$, we analyze the phenomenology of quark flavor-changing decays of the Higgs boson to a strange-bottom quark pair. We assume that the lightest CP-even Higgs boson, denoted as h , is the SM-like Higgs boson discovered by the LHC. A significant focus of this paper is to analyze the $U(1)_X\text{SSM}$ contributions to $h \rightarrow bs$.

From the perspective of the magnitude of $\text{Br}(h \rightarrow bs)$ and data analysis, the $\text{Br}(h \rightarrow bs)$ can reach the order of 10^{-3} , which is four orders of magnitude larger than the SM prediction. We consider the Feynman diagrams for the $h \rightarrow bs$ process and perform extensive calculations, plotting linear graphs of various parameters versus $\text{Br}(h \rightarrow bs)$. To enhance the fitting degree of the numerical analysis, we include χ^2 and conduct a broad scan of the parameters. Through numerical analysis, we find that a subset of parameters exert a significant influence on the results. M_1 , M_2 , M_{BL} , $M_{BB'}$, and M_D^2 are the insensitive parameters, while g_X , g_{YX} , $\tan \beta$, and λ_H are the sensitive parameters. Finally, we analyze the relationship between Δa_μ and other sensitive parameters, as well as the correlation between Δa_μ and $\text{Br}(h \rightarrow bs)$. Through comprehensive research, we have demonstrated that all parameters in our work satisfy the constraints from $h \rightarrow bs$ process. However, such decays remain undetectable at the LHC[53, 54]. It may be detected at ILC in the future. We believe that our findings may serve as a valuable resource for those interesting decays within alternative frameworks of new physics.

Acknowledgments

This work is supported by National Natural Science Foundation of China (NNSFC)(No.12075074), Natural Science Foundation of Hebei Province(A2020201002, A2023201040, A2022201022, A2022201017, A2023201041), Natural Science Foundation of Hebei Education Department (QN2022173), Post-graduate's Innovation Fund Project of Hebei University (HBU2024SS042), the youth top-notch talent support program of the Hebei Province.

Appendix A: Used mass matrices and coupling vertices in $U(1)_X$ SSM

At the tree level, the mass-squared matrix for the CP-even Higgs $(\phi_d, \phi_u, \phi_\eta, \bar{\phi}_\eta, \phi_s)$ is as follows

$$M_h^2 = \begin{pmatrix} m_{\phi_d\phi_d} & m_{\phi_u\phi_d} & m_{\phi_\eta\phi_d} & m_{\bar{\phi}_\eta\phi_d} & m_{\phi_s\phi_d} \\ m_{\phi_d\phi_u} & m_{\phi_u\phi_u} & m_{\phi_\eta\phi_u} & m_{\bar{\phi}_\eta\phi_u} & m_{\phi_s\phi_u} \\ m_{\phi_d\phi_\eta} & m_{\phi_u\phi_\eta} & m_{\phi_\eta\phi_\eta} & m_{\bar{\phi}_\eta\phi_\eta} & m_{\phi_s\phi_\eta} \\ m_{\phi_d\bar{\phi}_\eta} & m_{\phi_u\bar{\phi}_\eta} & m_{\phi_\eta\bar{\phi}_\eta} & m_{\bar{\phi}_\eta\bar{\phi}_\eta} & m_{\phi_s\bar{\phi}_\eta} \\ m_{\phi_d\phi_s} & m_{\phi_u\phi_s} & m_{\phi_\eta\phi_s} & m_{\bar{\phi}_\eta\phi_s} & m_{\phi_s\phi_s} \end{pmatrix}, \quad (\text{A1})$$

$$m_{\phi_d\phi_d} = m_{H_d}^2 + \mu^2 + \frac{1}{8} \left([g_1^2 + (g_X + g_{YX})^2 + g_2^2] (3v_d^2 - v_u^2) + 2(g_{YX}g_X + g_X^2)(v_\eta^2 - v_{\bar{\eta}}^2) \right) + \sqrt{2}v_S\mu\lambda_H + \frac{1}{2}(v_u^2 + v_S^2)\lambda_H^2, \quad (\text{A2})$$

$$m_{\phi_d\phi_u} = -\frac{1}{4} \left(g_2^2 + (g_{YX} + g_X)^2 + g_1^2 \right) v_d v_u + \lambda_H^2 v_d v_u - \lambda_H l_W - \frac{1}{2} \lambda_H v_\eta v_{\bar{\eta}} \lambda_C + v_S^2 \kappa - B_\mu - \sqrt{2}v_S \left(\frac{1}{2} T_{\lambda_H} + M_S \lambda_H \right), \quad (\text{A3})$$

$$m_{\phi_u\phi_u} = m_{H_u}^2 + \mu^2 + \frac{1}{8} \left\{ \left([g_1^2 + (g_X + g_{YX})^2 + g_2^2] (3v_u^2 - v_d^2) + 2(g_{YX}g_X + g_X^2)(v_\eta^2 - v_{\bar{\eta}}^2) \right) \right\} + \sqrt{2}v_S\mu\lambda_H + \frac{1}{2}(v_d^2 + v_S^2)\lambda_H^2, \quad (\text{A4})$$

$$m_{\phi_d\phi_\eta} = \frac{1}{2}g_X(g_{YX} + g_X)v_d v_\eta - \frac{1}{2}v_u v_{\bar{\eta}} \lambda_H \lambda_C, \quad (\text{A5})$$

$$m_{\phi_u\phi_\eta} = -\frac{1}{2}g_X(g_{YX} + g_X)v_d v_\eta - \frac{1}{2}v_d v_{\bar{\eta}} \lambda_H \lambda_C, \quad (\text{A6})$$

$$m_{\phi_\eta\phi_\eta} = m_\eta^2 + \frac{1}{4} \left([(g_{YX}g_X + g_X^2)](v_d^2 - v_u^2) + 2g_X^2(3v_\eta^2 - v_{\bar{\eta}}^2) \right) + \frac{\lambda_C^2}{2}(v_\eta^2 + v_S^2), \quad (\text{A7})$$

$$m_{\phi_d\bar{\phi}_\eta} = -\frac{1}{2}g_X(g_{YX} + g_X)v_d v_\eta - \frac{1}{2}v_u v_{\bar{\eta}} \lambda_H \lambda_C, \quad (\text{A8})$$

$$m_{\phi_u\bar{\phi}_\eta} = \frac{1}{2}g_X(g_{YX} + g_X)v_d v_\eta - \frac{1}{2}v_d v_{\bar{\eta}} \lambda_H \lambda_C, \quad (\text{A9})$$

$$m_{\phi_\eta\bar{\phi}_\eta} = (\lambda_C^2 - g_X^2)v_\eta v_{\bar{\eta}} + \frac{\lambda_C}{2}(2l_W - \lambda_H v_d v_u) + \frac{v_S}{\sqrt{2}}(2M_S \lambda_C + T_{\lambda_C}) + \frac{v_S^2}{2}\lambda_C \kappa, \quad (\text{A10})$$

$$m_{\bar{\phi}_\eta\bar{\phi}_\eta} = m_{\bar{\eta}}^2 + \frac{1}{4} \left((g_{YX}g_X + g_X^2)(v_u^2 - v_d^2) + 2g_X^2(3v_{\bar{\eta}}^2 - v_\eta^2) \right) + \frac{\lambda_C^2}{2}(v_\eta^2 + v_S^2), \quad (\text{A11})$$

$$m_{\phi_d\phi_s} = \left(\lambda_H v_d v_S + \sqrt{2}v_d \mu - v_u(\kappa v_S + \sqrt{2}M_S) \right) \lambda_H - \frac{1}{\sqrt{2}}v_u T_{\lambda_H}, \quad (\text{A12})$$

$$m_{\phi_u\phi_s} = \left(\lambda_H v_u v_S + \sqrt{2}v_u \mu - v_d(\kappa v_S + \sqrt{2}M_S) \right) \lambda_H - \frac{1}{\sqrt{2}}v_d T_{\lambda_H}, \quad (\text{A13})$$

$$m_{\phi_\eta\phi_s} = \left(\lambda_C v_\eta v_S + v_{\bar{\eta}}(\kappa v_S + \sqrt{2}M_S) \right) \lambda_C + \frac{1}{\sqrt{2}}v_{\bar{\eta}} T_{\lambda_C}, \quad (\text{A14})$$

$$m_{\phi_{\bar{\eta}}\phi_s} = \left(\lambda_C v_{\bar{\eta}} v_S + v_{\eta} (\kappa v_S + \sqrt{2} M_S) \right) \lambda_C + \frac{1}{\sqrt{2}} v_{\eta} T_{\lambda_C}, \quad (\text{A15})$$

$$m_{\phi_s\phi_s} = m_S^2 + \left(2l_W + 3v_S (\kappa v_S + 2\sqrt{2} M_S) + \lambda_C v_{\eta} v_{\bar{\eta}} - \lambda_H v_d v_u \right) \kappa + 2B_S \\ + \frac{1}{2} \lambda_C^2 \xi^2 + \frac{1}{2} \lambda_H^2 v^2 + 4M_S^2 + \sqrt{2} v_S T_{\kappa}. \quad (\text{A16})$$

This matrix is diagonalized by Z^H

$$Z^H M_h^2 Z^{H,\dagger} = M_{2,h}^{dia}. \quad (\text{A17})$$

The mass matrix for charginos in the basis: $(\tilde{W}^-, \tilde{H}_d^-), (\tilde{W}^+, \tilde{H}_u^+)$

$$M_{\chi^{\pm}} = \begin{pmatrix} M_2 & \frac{1}{\sqrt{2}} g_2 v_u \\ \frac{1}{\sqrt{2}} g_2 v_d & \frac{1}{\sqrt{2}} \lambda_H v_S + \mu \end{pmatrix}, \quad (\text{A18})$$

The matrix is diagonalized by U and V

$$U^* M_{\chi^{\pm}} V^{\dagger} = M_{\chi^{\pm}}^{dia}. \quad (\text{A19})$$

The mass squared matrix for up-squarks $(\tilde{u}_L^0, \tilde{u}_R^0)$ reads

$$M_{\tilde{U}}^2 = \begin{pmatrix} m_{\tilde{u}_L^0 \tilde{u}_L^{0,*}} & m_{\tilde{u}_R^0 \tilde{u}_L^{0,*}}^{\dagger} \\ m_{\tilde{u}_L^0 \tilde{u}_R^{0,*}} & m_{\tilde{u}_R^0 \tilde{u}_R^{0,*}} \end{pmatrix}, \quad (\text{A20})$$

$$m_{\tilde{u}_L^0 \tilde{u}_L^{0,*}} = \frac{1}{24} \left(3g_2^2 (-v_u^2 + v_d^2) + (g_1^2 + g_{YX}^2) (-v_d^2 + v_u^2) \right. \\ \left. + g_{YX} g_X (2v_{\bar{\eta}}^2 - 2v_{\eta}^2 - v_d^2 + v_u^2) \right) + \frac{1}{2} (2m_{\tilde{Q}}^2 + v_u^2 Y_u^{\dagger} Y_u), \quad (\text{A21})$$

$$m_{\tilde{u}_L^0 \tilde{u}_R^{0,*}} = -\frac{1}{2} \left(\sqrt{2} (v_d Y_u \mu^* - v_u T_u) + v_d v_S Y_u \lambda_H^* \right), \quad (\text{A22})$$

$$m_{\tilde{u}_R^0 \tilde{u}_R^{0,*}} = \frac{1}{24} \left(4(g_1^2 + g_{YX}^2) (-v_u^2 + v_d^2) + g_{YX} g_X (7v_d^2 - 7v_u^2 - 8v_{\bar{\eta}}^2 + 8v_{\eta}^2) \right. \\ \left. + 3g_X^2 (-2v_{\bar{\eta}}^2 + 2v_{\eta}^2 - v_u^2 + v_d^2) \right) + \frac{1}{2} (2m_{\tilde{U}}^2 + v_u^2 Y_u Y_u^{\dagger}). \quad (\text{A23})$$

The mass squared matrix for down-squarks $(\tilde{d}_L^0, \tilde{d}_R^0)$ reads

$$M_{\tilde{D}}^2 = \begin{pmatrix} m_{\tilde{d}_L^0 \tilde{d}_L^{0,*}} & m_{\tilde{d}_R^0 \tilde{d}_L^{0,*}}^{\dagger} \\ m_{\tilde{d}_L^0 \tilde{d}_R^{0,*}} & m_{\tilde{d}_R^0 \tilde{d}_R^{0,*}} \end{pmatrix}, \quad (\text{A24})$$

$$m_{\tilde{d}_L^0 \tilde{d}_L^{0,*}} = \frac{1}{24} \left((3g_2^2 + g_1^2 + g_{YX}^2) (-v_d^2 + v_u^2) + g_{YX} g_X (2v_{\bar{\eta}}^2 - 2v_{\eta}^2 - v_d^2 + v_u^2) \right)$$

$$+\frac{1}{2}(2m_{\tilde{Q}}^2 + v_d^2 Y_d^\dagger Y_d), \quad (\text{A25})$$

$$m_{\tilde{d}_L^0 \tilde{d}_R^{0,*}} = -\frac{1}{2} \left(\sqrt{2}(-v_d T_d + v_u Y_d \mu^*) + v_u v_S Y_d \lambda_H^* \right), \quad (\text{A26})$$

$$m_{\tilde{d}_R^0 \tilde{d}_R^{0,*}} = \frac{1}{24} \left(2(g_1^2 + g_{YX}^2)(-v_u^2 + v_d^2) + g_{YX} g_X (-4v_{\tilde{\eta}}^2 + 4v_{\tilde{\eta}}^2 + 5v_d^2 - 5v_u^2) \right. \\ \left. + 3g_X^2(-2v_{\tilde{\eta}}^2 + 2v_{\tilde{\eta}}^2 - v_u^2 + v_d^2) \right) + \frac{1}{2}(2m_{\tilde{D}}^2 + v_d^2 Y_d Y_d^\dagger). \quad (\text{A27})$$

The mass matrix for neutralino in the basis $(\lambda_{\tilde{B}}, \tilde{W}^0, \tilde{H}_d^0, \tilde{H}_u^0, \lambda_{\tilde{X}}, \tilde{\eta}, \tilde{\eta}, \tilde{s})$ is

$$M_{\tilde{\chi}^0} = \begin{pmatrix} M_1 & 0 & -\frac{g_1}{2}v_d & \frac{g_1}{2}v_u & M_{BB'} & 0 & 0 & 0 \\ 0 & M_2 & \frac{g_2}{2}v_d & -\frac{g_2}{2}v_u & 0 & 0 & 0 & 0 \\ -\frac{g_1}{2}v_d & \frac{g_2}{2}v_d & 0 & m_{\tilde{H}_d^0 \tilde{H}_d^0} & m_{\lambda_{\tilde{X}} \tilde{H}_d^0} & 0 & 0 & -\frac{\lambda_H v_u}{\sqrt{2}} \\ \frac{g_1}{2}v_u & -\frac{g_2}{2}v_u & m_{\tilde{H}_d^0 \tilde{H}_u^0} & 0 & m_{\lambda_{\tilde{X}} \tilde{H}_u^0} & 0 & 0 & -\frac{\lambda_H v_d}{\sqrt{2}} \\ M_{BB'} & 0 & m_{\tilde{H}_d^0 \lambda_{\tilde{X}}} & m_{\tilde{H}_u^0 \lambda_{\tilde{X}}} & M_{BL} & -g_X v_{\tilde{\eta}} & g_X v_{\tilde{\eta}} & 0 \\ 0 & 0 & 0 & 0 & -g_X v_{\tilde{\eta}} & 0 & \frac{1}{\sqrt{2}} \lambda_C v_S & \frac{1}{\sqrt{2}} \lambda_C v_{\tilde{\eta}} \\ 0 & 0 & 0 & 0 & g_X v_{\tilde{\eta}} & \frac{1}{\sqrt{2}} \lambda_C v_S & 0 & \frac{1}{\sqrt{2}} \lambda_C v_{\tilde{\eta}} \\ 0 & 0 & -\frac{1}{\sqrt{2}} \lambda_H v_u & -\frac{1}{\sqrt{2}} \lambda_H v_d & 0 & \frac{1}{\sqrt{2}} \lambda_C v_{\tilde{\eta}} & \frac{1}{\sqrt{2}} \lambda_C v_{\tilde{\eta}} & m_{\tilde{s}\tilde{s}} \end{pmatrix}, \quad (\text{A28})$$

$$m_{\tilde{H}_d^0 \tilde{H}_u^0} = -\frac{1}{\sqrt{2}} \lambda_H v_S - \mu, \quad m_{\tilde{H}_d^0 \lambda_{\tilde{X}}} = -\frac{1}{2} (g_{YX} + g_X) v_d, \\ m_{\tilde{H}_u^0 \lambda_{\tilde{X}}} = \frac{1}{2} (g_{YX} + g_X) v_u, \quad m_{\tilde{s}\tilde{s}} = 2M_S + \sqrt{2} \kappa v_S. \quad (\text{A29})$$

The mass matrix for charged Higgs in the basis: $(H_d^-, H_u^{+,*}), (H_d^{-,*}, H_u^+)$

$$M_{H^\pm}^2 = \begin{pmatrix} m_{H_d^- H_d^{-,*}} & m_{H_u^{+,*} H_d^{-,*}} \\ m_{H_d^- H_u^+} & m_{H_u^{+,*} H_u^+} \end{pmatrix}, \quad (\text{A30})$$

$$m_{H_d^- H_d^{-,*}} = \frac{1}{8} \left((g_2^2 + g_X^2) v_d^2 + (g_2^2 - g_X^2) v_u^2 + (g_1^2 + g_{YX}^2) (v_d^2 - v_u^2) - 2g_X^2 v_{\tilde{\eta}}^2 \right. \\ \left. + 2[g_{YX} g_X (v_d^2 + v_{\tilde{\eta}}^2 - v_{\tilde{\eta}}^2 - v_u^2) + g_X^2 v_{\tilde{\eta}}^2] \right) \\ + \left(|\mu|^2 + \sqrt{2} v_S \Re(\mu \lambda_H^*) + \frac{1}{2} v_S^2 |\lambda_H|^2 \right), \quad (\text{A31})$$

$$m_{H_d^- H_u^+} = \frac{1}{2} \left(2(\lambda_H l_W^* + B_\mu) + \lambda_H (2\sqrt{2} v_S M_S^* - v_d v_u \lambda_H^* + v_{\tilde{\eta}} v_{\tilde{\eta}} \lambda_C^* \right. \\ \left. + \sqrt{2} v_S T_{\lambda_H}) \right) + \frac{1}{4} g_2^2 v_d v_u, \quad (\text{A32})$$

$$m_{H_u^{+,*} H_u^+} = \frac{1}{8} \left((g_2^2 - g_X^2) v_d^2 + (g_2^2 + g_X^2) v_u^2 + (g_1^2 + g_{YX}^2) (v_u^2 - v_d^2) - 2g_X^2 v_{\tilde{\eta}}^2 \right. \\ \left. + 2[g_{YX} g_X (v_u^2 + v_{\tilde{\eta}}^2 - v_d^2 - v_{\tilde{\eta}}^2) + g_X^2 v_{\tilde{\eta}}^2] \right) \\ + \frac{1}{2} \left(2|\mu|^2 + 2\sqrt{2} v_S \Re(\mu \lambda_H^*) + v_S^2 |\lambda_H|^2 \right). \quad (\text{A33})$$

Here, we present some couplings required in this model

$$\mathcal{L}_{\chi^+ d\bar{u}^*} = \sum_{a=1}^3 \bar{\chi}_i^+ \left((-g_2 V_{i1}^* Z_{ka}^U + V_{i2}^* Y_{u,a} Z_{k3+a}^U) P_L + (Y_{d,a}^* Z_{ka}^U U_{i2}) P_R \right) d_{j\beta} \tilde{u}_{k\gamma}^* C_{ja}, \quad (\text{A34})$$

$$\mathcal{L}_{\chi^0 d\bar{d}^*} = -\frac{1}{6} \bar{\chi}_i^0 \left\{ (\sqrt{2} g_1 N_{i1}^* Z_{ka}^D - 3\sqrt{2} g_2 N_{i2}^* Z_{ka}^D + \sqrt{2} g_{YX} N_{i5}^* Z_{ka}^D + 6N_{i3}^* Y_{d,a} Z_{k3+a}^D) P_L + \right. \\ \left. (6Y_{d,a}^* Z_{kb}^D N_{i3} + \sqrt{2} Z_{k3+a}^D [2g_1 N_{i1} + (2g_{YX} + 3g_X) N_{i5}]) P_R \right\} d_{j\beta} \tilde{d}_{k\gamma}^*, \quad (\text{A35})$$

$$\mathcal{L}_{hH^- W^+} = \frac{1}{2} g_2 h_i \left(Z_{i1}^H Z_{j1}^- - Z_{i2}^H Z_{j2}^- \right) \left(-p_\mu^{H_j^-} + p_\mu^{h_i} \right) H_j^- W_\mu^+, \quad (\text{A36})$$

$$\mathcal{L}_{hW^+ W^-} = \frac{1}{2} g_2^2 h_i \left(v_d Z_{i1}^H + v_u Z_{i2}^H \right) g_{\sigma\mu} W_\sigma^+ W_\mu^-. \quad (\text{A37})$$

Here $P_L = \frac{1-\gamma^5}{2}$, $P_R = \frac{1+\gamma^5}{2}$, N , Z^D and Z^U , are the diagonalizing matrices for M_{χ^0} , $M_{\tilde{D}}^2$ and $M_{\tilde{U}}^2$. They satisfy the relations $N^T M_{\chi^0} N = \text{diag}(m_{\chi_1^0}, m_{\chi_2^0}, \dots, m_{\chi_8^0})$ and $Z_{\tilde{D}(\tilde{U})}^\dagger M_{\tilde{D}(\tilde{U})}^2 Z_{\tilde{D}(\tilde{U})} = \text{diag}(m_{\tilde{d}(\tilde{u})_1}^2, m_{\tilde{d}(\tilde{u})_2}^2, \dots, m_{\tilde{d}(\tilde{u})_6}^2)$, where $m_{\chi_i^0}$ ($i = 1, 2, \dots, 8$) and $m_{\tilde{d}(\tilde{u})_i}^2$ ($i = 1, 2, \dots, 6$) denote the corresponding mass eigenvalues of M_{χ^0} and $M_{\tilde{D}(\tilde{U})}^2$.

Appendix B: Feynman amplitude calculation process

We initially address the resolution of the Feynman integral, utilizing the formula specified in Ref.[55] for the integration of the denominator

$$\frac{1}{ABC} = \int_0^1 dx \int_0^1 2ydy \frac{1}{[(Ax + B(1-x))y + C(1-y)]^3}. \quad (\text{B1})$$

Performing the integral calculation in this manner can significantly enhance the efficiency of numerical computations in our work. Based on Eq.(B1), we arrive at

$$\int_0^1 dx \int_0^1 2ydy \left\{ \left([(k+q)^2 - m_{\chi^0}^2]x + (k^2 - m_{d_j}^2)(1-x) \right) y \right. \\ \left. + (k^2 + p^2 + q^2 - m_{d_i}^2)(1-y) \right\}^{-3} \\ = \int_0^1 dx \int_0^1 2ydy \frac{1}{(k'^2 - J)^3}. \quad (\text{B2})$$

The needed expressions are

$$(p+q)xy + q(1-y) = T, \\ k + T = k', \\ J = -p^2 xy + q^2 [xy + (1-y)]^2 + 2p \cdot q [xy(xy-y)] + xy + (1-y) \\ + m_{\chi^0}^2 (1-y) + m_{d_i}^2 xy + m_{d_j}^2 (1-y)y. \quad (\text{B3})$$

Subsequently, we utilize D–dimensional spatial integration to perform relevant calculations on the denominators

$$\int \frac{d^D k'}{(2\pi)^D} \frac{(k^2)^\alpha}{(k^2 - R^2)^\beta} = i \frac{(-1)^{\alpha-\beta} \Gamma(1 + \frac{D}{2}) \Gamma(\beta - \alpha - \frac{D}{2})}{(4\pi)^{\frac{D}{2}} \Gamma(\frac{D}{2}) \Gamma(\beta) (R^2)^{\beta-\alpha-\frac{D}{2}}}. \quad (\text{B4})$$

We use dimensional regularization to handle divergent terms, where $d = 4 - 2\epsilon$ and take the limit as d approaches 4. To obtain finite results, the divergent terms are canceled out by the modified minimal subtraction (\overline{MS}) scheme.

The final integral result we get is

$$\begin{aligned} \mathcal{M}_{(a)} = & \int_0^1 dx \int_0^1 2y dy \left(\frac{-A_L B_L m_{\chi^0} - A_L B_R m_b xy - A_L B_R m_s xy + A_L B_R m_s y}{64\pi^2 J} \right) C_1 \gamma^5 \\ & + \frac{m_b A_L B_R C_1 xy}{64\pi^2 J} + m_s C_1 \frac{A_L B_R xy - A_L B_R y}{64\pi^2 J} + \frac{m_{\chi^0} A_L B_L C_1}{64\pi^2 J} + (L \rightarrow R). \end{aligned} \quad (\text{B5})$$

We process all the diagrams in Fig.1 according to the aforementioned methods and further simplify them.

Due to the immense complexity of the calculations involved, we employ *Mathematica* \ll *HighEnergyPhysics'FeynCalc'* package for analytical computations. We derive the Feynman amplitudes for all the diagrams, and use the on–shell condition for the external particles $p^2 = m_b^2$, $q^2 = m_s^2$, $(p + q)^2 = m_h^2$. Subsequently, we perform summation operations and compute the squared modulus of the amplitudes, denoted as $|\mathcal{M}|^2$.

-
- [1] ATLAS Publications, Phys. Lett. B **716** (2022) 1-29. [arXiv: 1207.7214].
 - [2] CMS Collaboration, Phys. Lett. B **716** (2012) 30-61. [arXiv: 1207.7235].
 - [3] J. Ren, R. Q. Xiao, M. Zhou, et al., JHEP **06** (2018) 090. [arXiv: 1706.05980].
 - [4] H. Sun, Y. J. Zhou, JHEP **11** (2012) 127. [arXiv: 1211.6201].
 - [5] M. Ibe, S. Matsumoto, T. T. Yanagida, Phys. Rev. D **85** (2012) 095011. [arXiv: 1202.2253].
 - [6] J. L. Evans, M. Ibe, S. Shirai, et al., Phys. Rev. D **85** (2012) 095004. [arXiv: 1201.2611].
 - [7] T. Moroi, K. Nakayama, Phys. Lett. B **710** (2012) 159-163. [arXiv: 1112.3123].
 - [8] F. Arco, S. Heinemeyer, M. J. Herrero (2023). [arXiv: 2306.07958].
 - [9] R. S. Willey, H. L. Yu, Phys. Rev. D **26** (1982) 3086-3091.
 - [10] L. G. Benitez-Guzmán, I. García-Jiménez, M. A. López-Osorio, et al., J. Phys. G **42** (2015) 085002. [arXiv: 1506.02718].

- [11] J. I. Aranda, G. González-Estrada, J. Montaña, et al., *J. Phys. G* **47** (2020) 125001. [arXiv: 2009.07166].
- [12] G. Blankenburg, J. Ellis, G. Isidori, *Phys. Lett. B* **712** (2012) 386-390. [arXiv: 1202.5704].
- [13] D. Barducci, A. J. Helmboldt, et al., *JHEP* **12** (2017) 105. [arXiv: 1710.06657].
- [14] C. X. Liu, H. B. Zhang, J. L. Yang, et al., *JHEP* **04** (2020) 002. [arXiv: 2002.04370].
- [15] H. B. Zhang, T. F. Feng, G. H. Luo, et al., *JHEP* **07** (2013) 069. [arXiv: 1305.4352].
- [16] S. M. Zhao, T. F. Feng, X. X. Dong, et al., *Nucl. Phys. B* **910** (2016) 225-239. [arXiv: 1603.09505].
- [17] S. Davidson, S. F. King, *Phys. Lett. B* **445** (1998) 191-198. [arXiv: 9808296].
- [18] S. M. Zhao, L. H. Su, X. X. Dong, et al., *JHEP* **03** (2022) 101.
- [19] B. Yan, S. M. Zhao, T. F. Feng, et al., *Nucl. Phys. B* **975** (2022) 115671. [arXiv: 2011.08533].
- [20] S. M. Zhao, T. F. Feng, M. J. Zhang, et al., *JHEP* **02** (2020) 130. [arXiv: 1905.11007].
- [21] M. Y. Liu, S. M. Zhao, S. Gao, et al., (2024). [arXiv: 2405.00961].
- [22] Y. T. Wang, S. M. Zhao, T. T. Wang., et al., *Phys. Rev. D* **106** (2022) 055044. [arXiv: 2207.01770].
- [23] S. M. Zhao, G. Z. Ning, J. J. Feng, et al., *Nucl. Phys. B* **969** (2021) 115469.
- [24] R. El-Kosseifi, J. L. Kneur, G. Moulataka, et al., *Eur. Phys. J. C* **82** (2022) 657. [arXiv: 2202.06919].
- [25] L. H. Su, S. M. Zhao, X. X. Dong, et al., *Eur. Phys. J. C* **81** (2021) 433 [arXiv: 2012.04824].
- [26] F. Abu-Ajamieh, M. Frasca, S. K. Vempati, *JHEP* **02** (2016) 075010 [arXiv:2305.17362].
- [27] R. K. Barman, P. S. B. Dev, A. Thapa, *Phys. Rev. D* **107** (2023) 075018 [arXiv:2210.16287].
- [28] R. Aaij, et al., *Eur. Phys. J. C* **78** (2028) 1008 [arXiv:1808.07135].
- [29] ATLAS Publications, *JHEP* **07** (2023) 166 [arXiv:2302.05225].
- [30] M. Badziak, G. Grilli di Cortona, M. Tabet, et al., *JHEP* **10** (2021) 181 [arXiv:2107.09708].
- [31] J. J. Zhang, M. He, X. G. He, et al., *JHEP* **02** (2019) 007 [arXiv:1807.00921].
- [32] CMS Collaboration, *Phys. Rev. D* **108** (2023) 072004 [arXiv:2305.18106].
- [33] ATLAS Collaboration, *JHEP* **07** (2023) 166 [arXiv:1907.05900].
- [34] J. H. Garcia, M. Nebot, F. Rajec, et al., *JHEP* **02** (2020) 147 [arXiv: 1907.05900].
- [35] G. Blankenburg, J. Ellis, G. Isidori, *Phys. Lett. B* **712** (2012) 386-390 [arXiv: 1202.5704].
- [36] D. Barducci, A. J. Helmboldt, *JHEP* **12** (2017) 105[arXiv:1710.06657].
- [37] G. Bélanger, J. Da Silva, H. M. Tran, *Phys. Rev. D* **95** (2017) 115017 [arXiv: 1703.03275].

- [38] V. Barger, P. Fileviez Perez, S. Spinner, Phys. Rev. Lett. **102** (2009) 181802 [arXiv: 0812.3661].
- [39] P. H. Chankowski, S. Pokorski, J. Wagner, Eur. Phys. J. C **47** (2006) 187
- [40] S. M. Zhao, X. Wang, X. X. Dong, et al., Symmetry **14** (2022) 2153. [arXiv: 2209.07094].
- [41] D. de Florian, et al., doi:10.23731/CYRM-2017-002. [arXiv:1610.07922].
- [42] R.L. Workman, et al., (Particle Data Group), Prog. Theor. Exp. Phys. **2022** (2022) 083C01
- [43] Á. S. de Jesus, F. S. Queiroz, J. W. F. Valle, et al., (2024). [arXiv: 2312.03851].
- [44] D. P. Aguillard et al., Phys. Rev. Lett. **131** (2023) 161802. [arXiv: 2308.06230].
- [45] P. Cox, C .C. Han, T. T. Yanagida, Phys. Rev. D **104** (2021) 075035 [arXiv:2104.03290].
- [46] M. V. Beekveld, W. Beenakker, M. Schutten, et al., SciPost Phys. **11** (2021) 3, 049 [arXiv:2104.03245].
- [47] M. Chakraborti, L. Roszkowski, S. Trojanowski, JHEP **05** (2021) 252 [arXiv:2104.04458].
- [48] F. Wang, L. Wu, Y. Xiao, et al., Nucl. Phys. B **970** (2021) 115486 [arXiv:2104.03262].
- [49] M. Chakraborti, S. Heinemeyer, I. Saha, Eur. Phys. J. C **81** (2021) 12, 1114 [arXiv:2104.03287].
- [50] M. Endo, K. Hamaguchi, S. Iwamoto, et al., JHEP **07** (2021) 075 [arXiv:2104.03217].
- [51] D. P. Aguillard, et al. Phys. Rev. Lett. **131** (2023) 161802.
- [52] A. Datta, D. Marfatia, L. Mukherjee, Phys. Rev. D. **109** (2024) L031701.
- [53] G. Blankenburg, J. Ellis, G. Isidori, Phys. Lett. B **712** (2012) 386.
- [54] R. Harnik, J. Kopp, J. Zupan, JHEP **03** (2013) 026.
- [55] B. L. Yang, Quantum Field Theory: From Operators to Path Integrals, World Scientific Publishing Co. (1988).